Effect of Active Damping on Output Impedance of Three-Phase Grid-Connected Converter

Abstract—**LCL-filter is commonly used to attenuate the switching harmonics of grid-connected converters. LCL-filter creates resonances in the converter dynamics which shall be damped for ensuring robust performance of the converter. Active damping methods can be used to attenuate the resonant behavior effectively. Accordingly, the output impedance is affected and the grid-interaction sensitivity of the converter varies with the active damping design. In order to carry out impedance-based stability analysis or assessment of the harmonic rejection capability, an accurate analytical model to predict the output impedance is necessary. This paper investigates the output impedance properties of capacitor-current-feedback active damping, which are so far not considered thoroughly in the literature. The output impedance modification with the active damping design is explained, thus, the stability and harmonic rejection capability of the converter can be improved. Furthermore, in order to validate the model, experimental measurements of the output impedance with active damping are presented for the first time in literature.**

Index Terms—**Active damping, control design, impedance modeling, power system stability**

I. Introduction

GRID-CONNECTED inverters are widely used to transfer energy from renewable energy sources to the utility grids. LCL-filter is superior in attenuating the output current harmonics caused by the switching actions compared to simple L-type filter and is therefore commonly utilized [1]. However, the resonant peaking caused by the LCL-filter must be attenuated properly to preserve stability of the system and to prevent harmonic resonances from affecting the grid current.

Active damping (AD) is commonly used to mitigate the resonant behavior of the LCL-filter as it does not produce additional power losses [2]. However, extra system cost may appear due to the need of additional measurement circuitry. Multi-loop active damping methods involve a feedback from a system state variable, which is usually the filter-capacitor current [2]–[8] and it is employed in this paper.

Considering active damping, the condition where the resonant frequency of the LCL-filter (f_{res}) equals one-sixth of the sampling frequency (f_{s}) has been noticed to be critical for stability of a grid-connected converter [4], [6], [9], [10]. Accordingly, active damping design is dependent on the resonant-to-sampling-frequency-ratio and poorly designed active damping may create right half-plane (RHP) poles into the current control loop causing instability [3]–[5], [9]–[12]. Moreover, considerably different stability characteristics can be obtained for inverter-current-controlled and grid-current-controlled converters. It is shown that the inverter-current feedback (ICF) and grid-current feedback (GCF) converters have opposite stability characteristics regarding the system delay

[10], [13]. Consequently, active damping is not necessary for ICF converter when $f_{\mathrm{res}} < f_{\mathrm{s}}/6$ but required for stability when $f_{\mathrm{res}} > f_{\mathrm{s}}/6$. For the GCF converter, these are reversed.

The output impedance of a power electronics-based converter dictates its external stability. The instability sensitivity of the converter changes due to arbitrary behavior of the grid impedance, that is, the grid usually behaves as an inductance at higher frequencies but can also contain resonances near the fundamental grid frequency [14]. The instability sensitivity can be decreased, for a grid-feeding converter, by ensuring as high output impedance as possible which should also behave passively, i.e. the phase is restricted between $-90^{\mathrm{o}}...+90^{\mathrm{o}}$ [15], [16]. The analysis of impedance-based stability has gained increasing attention in recent publications [15], [17]–[25]. It has been observed that the phase-locked loop (PLL) induces non-passivity to the impedance below the fundamental frequency which cannot be eliminated [19], [21], [23], [26]. Grid-voltage feed-forward methods have been widely used to increase the magnitude of the output impedance, thus decreasing the risk for the impedance-based interactions [18], [22].

Even though the active damping is widely used technique in grid-connected applications, its effect on the output impedance has been so far overlooked in the literature. For example, active damping was utilized in [18], [22], [27], but neither its parametric influence on the output impedance was analyzed nor experimental measurements of the impedance were presented. Output impedance analysis with active damping was presented briefly in [28], however, the effect of the delay was neglected which hides important information regarding the ratio of the LCL-filter resonant and sampling frequency. Furthermore, the impedances were not verified experimentally in aforementioned paper. Lastly, active damping of DC-DC converter and its impedance properties were analyzed in [29], but the results are not applicable for DC-AC grid-connected converters with LCL-filters.

The main contribution of this paper is to present an accurate impedance model for a three-phase grid-connected inverter with active damping, valid for analysis in both frequency regions of $f_{\mathrm{res}} < f_{\mathrm{s}}/6$ and $f_{\mathrm{res}} > f_{\mathrm{s}}/6$. The model can be used to predict the impedance-based instability when connecting the converter to a grid with arbitrary impedance characteristics. Moreover, the harmonic-rejection capability can be accurately predicted by the model. The output impedance analysis provides a new aspect for the active damping design, which normally concentrates on the stability evaluation of the output current control loop. As the active damping design has a significant effect on the output impedance, the impedance analysis should be utilized in the control design for improved robustness.

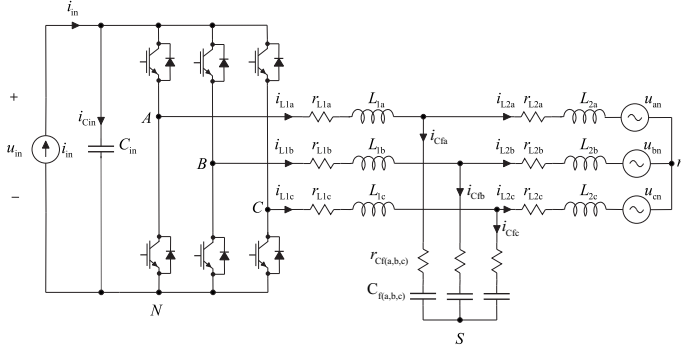The rest of the paper is organized as follows: small-signal

Fig. 1. Circuit diagram of a three-phase grid-connected VSI-based inverter.

TABLE I
OPERATING POINT AND COMPONENT VALUES.

Parameter	Value	Parameter	Value
U_{in}	415 V	C_{in}	1.9 mF
I_{in}	6.6 A	L_1	2.5 mH
$U_{\text{grid,rms}}$	120 V	r_{L2}	65 mΩ
$\omega_{\text{grid}}, \omega_{\text{s}}$	$2\pi 60$ rad/s	C_{f}	10 μF
f_{s}	6–8–20 kHz	r_{Cf}	10 mΩ
f_{res}	2.29 kHz	L_2	0.6 mH
$f_{\text{s}}/f_{\text{res}}$	2.6–3.5–8.7	r_{L1}	22 mΩ
r_{sw}	10 mΩ		

modeling and stability analysis of a three-phase PV inverter with active damping is shortly presented in Section II. Section III presents the output impedance analysis with different active damping feedback implementations. The analysis is verified by measurements from a 3-kW prototype in Section IV. Conclusions are drawn in Section V.

II. SMALL-SIGNAL MODELING WITH ACTIVE DAMPING

A. Overview

Fig. 1 shows the power-stage of the three-phase grid-connected inverter. According to Fig. 1 and small-signal modeling principles, the average-valued equations are derived and then linearized at a predefined operating point. The model is derived in the synchronous reference frame (i.e., in the dq-domain).

The system state-space can be generally presented as

$$
s\mathbf{X}(s) = \mathbf{A}\mathbf{X}(s) + \mathbf{B}\mathbf{U}(s)
$$
$$
\mathbf{Y}(s) = \mathbf{C}\mathbf{X}(s) + \mathbf{D}\mathbf{U}(s). \tag{1}
$$

The state-space matrices $\mathbf{A}$, $\mathbf{B}$, $\mathbf{C}$ and $\mathbf{D}$ are obtained from the linearized model and presented in Appendix A. Corresponding operating point and power-stage component values used in the forthcoming analysis are given in Table I.

From (1) the transfer function matrix between the input and the output variables can be solved as

$$
\mathbf{Y}(s) = \left[\mathbf{C}(s\mathbf{I} - \mathbf{A})^{-1}\mathbf{B} + \mathbf{D}\right]\mathbf{U}(s) = \mathbf{G}_{\text{H}}\mathbf{U}(s), \tag{2}
$$

where the vectors for linearized state, input and output variables are as given in (3) - (5), respectively.

$$
\mathbf{X}(s) = \left[\hat{i}_{\text{L1d}}, \hat{i}_{\text{L1q}}, \hat{i}_{\text{L2d}}, \hat{i}_{\text{L2q}}, \hat{u}_{\text{Cd}}, \hat{u}_{\text{Cq}}, \hat{u}_{\text{Cin}}\right]^{\text{T}}
$$
$$
= \left[\hat{\underline{i}}_{\text{L1}}, \hat{\underline{i}}_{\text{L2}}, \hat{\underline{u}}_{\text{C}}, \hat{u}_{\text{Cin}}\right]^{\text{T}} \tag{3}
$$

$$
\mathbf{U}(s) = \left[\hat{i}_{\text{in}}, \hat{u}_{\text{od}}, \hat{u}_{\text{oq}}, \hat{d}_{\text{d}}, \hat{d}_{\text{q}}\right]^{\text{T}} = \left[\hat{i}_{\text{in}}, \hat{\underline{u}}_{\text{o}}, \hat{\underline{d}}\right]^{\text{T}} \tag{4}
$$

$$
\mathbf{Y}(s) = \left[\hat{u}_{\text{in}}, \hat{i}_{\text{L1d}}, \hat{i}_{\text{L1q}}, \hat{i}_{\text{L2d}}, \hat{i}_{\text{L2q}}\right]^{\text{T}} = \left[\hat{i}_{\text{in}}, \hat{\underline{i}}_{\text{L1}}, \hat{\underline{i}}_{\text{L2}}\right]^{\text{T}} \tag{5}
$$

The system transfer function matrix $\mathbf{G}_{\text{H}}$ in (2) can be simplified and presented by using transfer matrices due to the inherent multivariable nature of the inverter [21], [30], [31]. By combining the d and q-components and their cross-coupling terms into two-by-two matrices, the transfer function matrix $\mathbf{G}_{\text{H}}$ in (2) can be expressed by

$$
\mathbf{G}_{\text{H}} = \begin{bmatrix} Z_{\text{in}} & \mathbf{T}_{\text{oi}} & \mathbf{G}_{\text{ci}} \\ \mathbf{G}_{\text{ioL}} & \mathbf{G}_{\text{oL}} & \mathbf{G}_{\text{cL}} \\ \mathbf{G}_{\text{io}} & \mathbf{Y}_{\text{o}} & \mathbf{G}_{\text{co}} \end{bmatrix}. \tag{6}
$$

Note that according to topological properties of the inverter in Fig. 1, the input voltage $\hat{u}_{\text{in}}$ and the input current $\hat{i}_{\text{in}}$ are scalar variables, hence, the input impedance Z_{in} in (6) is not a matrix. Explicit forms for transfer functions in (6) can be derived according to linear algebra with (2) and matrices (A.17) - (A.20).

The open-loop transfer functions in (6) can be used to form a control block diagram of the system by adding the necessary control functions, i.e., controllers, active damping feedback, delays and measurement gains. Accordingly, Fig. 2 shows the control block diagram of the output current and input voltage dynamics of a three-phase grid-connected inverter with active damping. Considering the block diagram and its transfer functions, 'VC' denotes the voltage control structure, 'CC' denotes the current control structure, 'AD' denotes the active damping and 'PLL' denotes the phase-locked loop. Note that the '-c' extension in variable $\hat{\underline{i}}_{\text{L1-c}}$ denotes the inverter current which is affected by the PLL. The PLL modeling has been done extensively e.g. in [19], [21], [26] regarding its effect on the system dynamics and, therefore, it is not considered further in this paper.

The system delay matrix $\mathbf{G}_{\text{del}}$ and active damping feedback gain matrix $\mathbf{G}_{\text{AD}}$ in Fig. 2 are as follows:

$$
\mathbf{G}_{\text{del}} = \begin{bmatrix} \frac{1 - k_1 s + k_2 s^2}{1 + k_1 s + k_2 s^2} & 0 \\ 0 & \frac{1 - k_1 s + k_2 s^2}{1 + k_1 s + k_2 s^2} \end{bmatrix} \tag{7}
$$

$$
\mathbf{G}_{\text{AD}} = \begin{bmatrix} \frac{R_{\text{d}}}{U_{\text{in}}} & 0 \\ 0 & \frac{R_{\text{d}}}{U_{\text{in}}} \end{bmatrix} \tag{8}
$$

In (7), a second order Padé approximation is used to replace ideal delay, i.e. $e^{-T_{\text{delay}}s}$, with $k_1 = 1/2T_{\text{d}}$ and $k_2 = 1/12T_{\text{d}}^2$. The system delay is chosen as $T_{\text{d}} = 1.5T_{\text{s}}$ where T_{s} is the sampling interval. This consists of PWM, AD sampling and
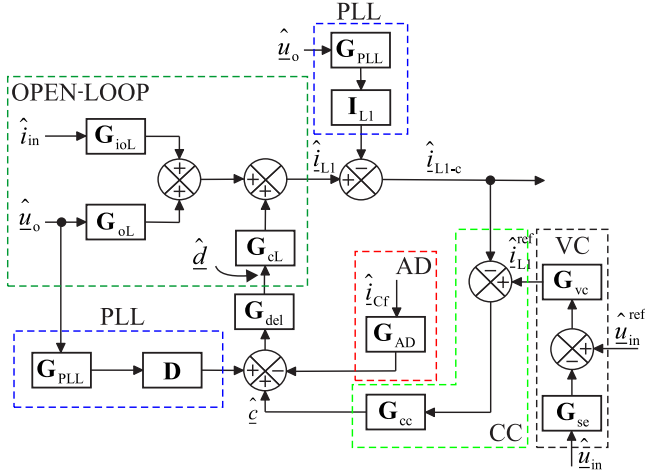
Fig. 2. Closed-loop block-diagram of output current dynamics with active damping in the dq-domain.
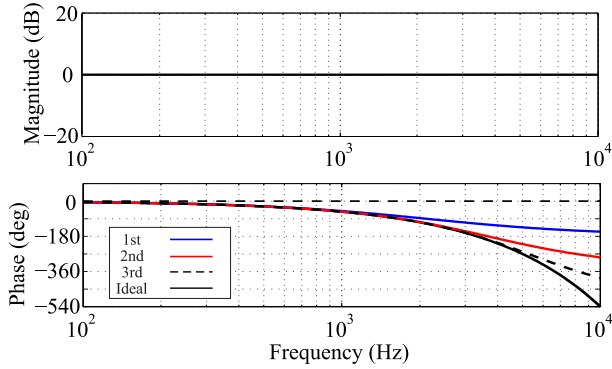

Fig. 3. Frequency-domain comparison of different Padé approximations.

processing delays and is commonly considered as an appropriate delay for DSP-based control systems [32]. It is worth noting that the Padé approximation is prone to inaccuracy depending on the order. However, as shown in Fig. 3 for $f_\mathrm{s} = 6$ kHz, the second-order approximation is accurate for up to half of the switching frequency which ensures sufficient accuracy of the model as can be verified from the experimental measurements.

B. Current Control Stability with Active Damping

Active damping feedback gain optimization has been presented for GCF converters in [3] with proportional capacitor current feedback. Furthermore, root locus methods have been popular for ICF converters when analyzing the stability with capacitor current or voltage feedback active damping [6], [7], [33]. In order to improve the system stability and robustness, high-pass-filtered (HPF) capacitor current feedback method has been proposed for GCF converters in [34] to compensate the phase-lag induced by the delay.

However, due to lack of explicit damping gain determination methods for three-phase ICF converters with both $f_\mathrm{res} < f_\mathrm{s}/6$ and $f_\mathrm{res} > f_\mathrm{s}/6$, root trajectories in the s-plane are used in this paper to determine boundaries for stable active damping feedback gains. Furthermore, they are subsequently used to analyze

the effect of root locations on the shape of output impedance. Here, the root trajectories are obtained by investigating the closed-loop transfer function matrix from the current reference to the output current, which is given by

$$\mathbf{G}_\mathrm{cL}^\mathrm{out} = \mathbf{G}_\mathrm{cL}^\mathrm{AD}(\mathbf{I} + \mathbf{L}_\mathrm{out})^{-1}\mathbf{L}_\mathrm{out}\left(\mathbf{G}_\mathrm{cL}^\mathrm{AD}\right)^{-1}. \tag{9}$$

The active-damping-affected control-to-inductor-current transfer function matrix $\mathbf{G}_\mathrm{cL}^\mathrm{AD}$ can be derived from Fig. 2 as given in (10). The current control loop gain matrix $\mathbf{L}_\mathrm{out}$ and PI-based current controller matrix $\mathbf{G}_\mathrm{cc}$ are given in (11) and (12), respectively.

$$\mathbf{G}_\mathrm{cL}^\mathrm{AD} = \mathbf{G}_\mathrm{cL}[\mathbf{I} + \mathbf{G}_\mathrm{del}\mathbf{G}_\mathrm{AD}(\mathbf{G}_\mathrm{cL} - \mathbf{G}_\mathrm{co})]^{-1} \tag{10}$$

$$\mathbf{L}_\mathrm{out} = \mathbf{G}_\mathrm{cc}\mathbf{G}_\mathrm{cL}^\mathrm{AD} \tag{11}$$

$$\mathbf{G}_\mathrm{cc} = \begin{bmatrix} K_\mathrm{p} + \frac{K_\mathrm{i}}{s} & 0 \\ 0 & K_\mathrm{p} + \frac{K_\mathrm{i}}{s} \end{bmatrix} \tag{12}$$

where $K_\mathrm{p} = 0.018$ and $K_\mathrm{i} = 22.4$.

As the high-frequency behavior between the d and q-component transfer functions regarding (9) is similar, only the former is used in the analysis for simplicity. Fig. 4 presents the root trajectories of (9) with varying virtual resistor value R_d and different active damping feedback implementations for both aforementioned resonant-to-sampling frequency ratios. It is shown that the HPF (Fig. 4(b)) clearly improves stability margins when $f_\mathrm{res} < f_\mathrm{s}/6$ (f_s = 20 kHz) compared with the proportional feedback in Fig. 4(a) as the roots are shifted farther to the left-half plane (LHP). When the sampling frequency is changed as $f_\mathrm{s}/6 < f_\mathrm{res} < f_\mathrm{s}/3$ (f_s = 8 kHz), the system is unstable with the used parameters by using a HPF as shown in Fig. 4(d), i.e. the poles are constantly in the RHP. By lowering the HPF cutoff frequency ($\omega_\mathrm{cutoff} = \omega_\mathrm{res} \to \omega_\mathrm{cutoff} = 0.5\omega_\mathrm{res}$) in Fig. 4(e), the stability can be recovered. However, the stability margins are still inferior compared to the proportional active damping feedback shown in Fig. 4(c).

Conversely, it was observed that low-pass filtering (LPF) the capacitor current improves the stability when $f_\mathrm{s}/6 < f_\mathrm{res} < f_\mathrm{s}/3$ (f_s = 8 kHz) as is demonstrated in Fig. 4(f). Accordingly, the system poles are shifted farther to the LHP, which yields more stable dynamics. Aforementioned behavior is caused by the system delay ($e^{-kT_\mathrm{s}s}$) as it affects the active damping feedback, which can be presented according to the Euler's formula by

$$G_\mathrm{AD} = R_\mathrm{d}/U_\mathrm{in}\left[\cos\left(kT_\mathrm{s}\omega\right) - j\sin\left(kT_\mathrm{s}\omega\right)\right] \tag{13}$$

where $k = 1.5$ in this case. Accordingly, the real part changes sign when $f_\mathrm{res} = f_\mathrm{s}/6$, and the active damping gain has to be inverted in order to preserve stability [4]. The imaginary part, on the other hand, changes its sign when $f_\mathrm{res} = f_\mathrm{s}/3$ and, therefore, it can be considered to induce either phase-lag or phase-boost depending on its sign. Consequently, the HPF is effective when $f_\mathrm{res} < f_\mathrm{s}/6$ or $f_\mathrm{s}/3 < f_\mathrm{res} < f_\mathrm{s}/2$ when imaginary part is negative, i.e., phase-boost is required.
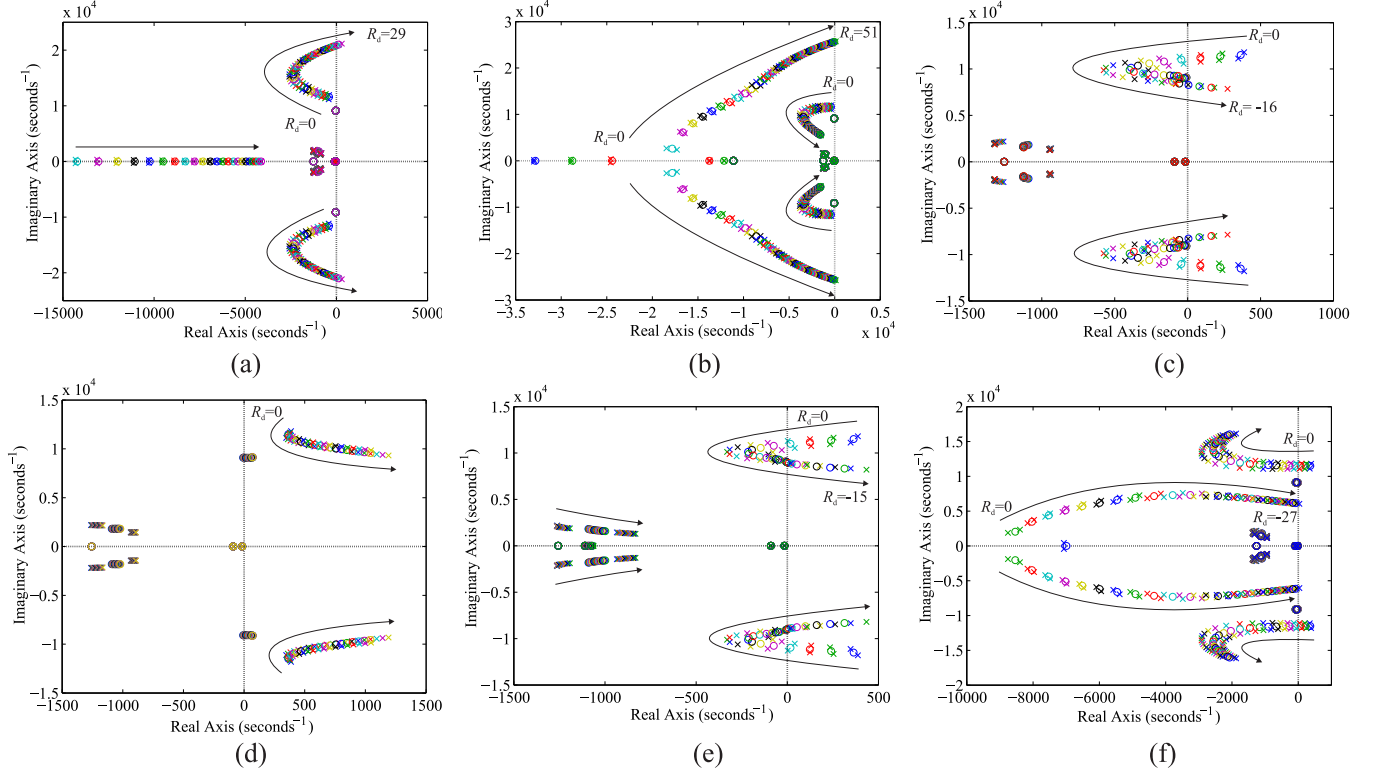
Fig. 4. Root trajectories of current control loop for different cases: (a) $f_\text{res} < f_\text{s}/6$ and proportional AD, (b) $f_\text{res} < f_\text{s}/6$ and HPF AD, (c) $f_\text{res} > f_\text{s}/6$ and proportional AD, (d) $f_\text{res} > f_\text{s}/6$ and high cutoff HPF AD, (e) $f_\text{res} > f_\text{s}/6$ and low cutoff HPF AD, (f) $f_\text{res} > f_\text{s}/6$ and LPF AD.
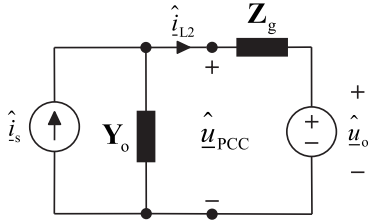

Fig. 5. Small-signal illustration of the grid-connected converter.

Conversely, the LPF should be utilized to induce phase-lag when $f_\text{s}/6 < f_\text{res} < f_\text{s}/3$ for improved stability characteristics as shown in Fig. 4(f).

III. OUTPUT IMPEDANCE ANALYSIS

For the stability analysis of the grid-interface, the output impedance of the converter and the grid impedance are considered. The interconnection can be represented as a small-signal impedance model as shown in Fig. 5.

Based on the small-signal equivalent circuit shown in Fig. 5, the output current vector $\hat{\underline{i}}_\text{L2}$ can be expressed as given in (14).

$$\hat{\underline{i}}_\text{L2} = [\mathbf{I} + \mathbf{Y}_\text{o}\mathbf{Z}_\text{g}]^{-1}\hat{\underline{i}}_\text{s} - [\mathbf{I} + \mathbf{Y}_\text{o}\mathbf{Z}_\text{g}]^{-1}\mathbf{Y}_\text{o}\hat{\underline{u}}_\text{o} \quad (14)$$

Stability can be evaluated by applying the generalized Nyquist stability criterion to the return-ratio matrix $\mathbf{Y}_\text{o}\mathbf{Z}_\text{g}$ [35].

For the impedance-based analysis, the closed-loop output admittance of the grid connected inverter can be given by

$$\mathbf{Y}_\text{o}^\text{tot} = \mathbf{Y}_\text{o}^\text{out} + \mathbf{G}_\text{co}^\text{out}\mathbf{G}_\text{vc}\mathbf{G}_\text{se}(\mathbf{I} + \mathbf{L}_\text{in})^{-1}\mathbf{T}_\text{oi}^\text{out} \quad (15)$$

where $\mathbf{G}_\text{vc}$ is the PI-based voltage controller matrix given by

$$\mathbf{G}_\text{vc} = \begin{bmatrix} K_\text{p} + \frac{K_\text{i}}{s} & 0 \\ 0 & 1 \end{bmatrix}. \quad (16)$$

For the voltage controller, $K_\text{p} = 0.36$ and $K_\text{i} = 4.47$. The DC-link control loop gain is given as $\mathbf{L}_\text{in} = \mathbf{G}_\text{ci}^\text{out}\mathbf{G}_\text{vc}\mathbf{G}_\text{se}$ and $\mathbf{I}$ is a unity matrix. $\mathbf{G}_\text{se}$ is the voltage sensing gain which is presumed to be unity. The transfer function matrices $\mathbf{Y}_\text{o}^\text{out}$, $\mathbf{G}_\text{ci}^\text{out}$, $\mathbf{G}_\text{co}^\text{out}$ and $\mathbf{T}_\text{oi}^\text{out}$ can be found in Appendix B. The superscript 'tot' denotes that the DC-link voltage control loop is closed. The admittance matrix in (15) yields the direct and quadrature components as well as the cross-coupling admittances. Note that in the forthcoming analysis, the admittance is expressed as impedance by $Z = 1/Y$.

A. Output Impedance for $f_\text{res} < f_\text{s}/6$

Fig. 6 presents the predicted d-component of the output impedance when $f_\text{res} < f_\text{s}/6$ and $R_\text{d} = [5, 15, 27]$. Note that only the d-component is shown in Figs. 6 - 11 for simplicity since the active damping affects the high frequency (>100 Hz) behavior which is identical between the d and q-components.

It is shown in Fig. 6 that the impedance magnitude and shape at the resonant frequency vary as the virtual resistor value is modified. First, by increasing the virtual resistor from $R_\text{d} = 5$ (solid line) to $R_\text{d} = 15$ (dashed line), the magnitude of the impedance at the resonant frequency increases from 4
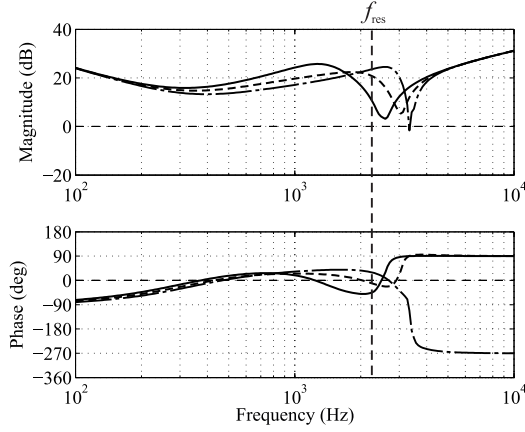
Fig. 6. Predicted d-component of the output impedance with $R_{\rm d}$= 5 (solid line), $R_{\rm d}$= 15 (dashed line) and $R_{\rm d}$= 27 (dash-dotted line).

Fig. 7. Predicted d-component of the output impedance with HPF $R_{\rm d}$= 5 (solid line), $R_{\rm d}$= 15 (dashed line) and $R_{\rm d}$= 27 (dash-dotted line), $\omega_{\rm cutoff} = \omega_{\rm res}$.

Fig. 8. Predicted d-component of the output impedance with $R_{\rm d}$= -5 (solid line), $R_{\rm d}$= -10 (dashed line) and $R_{\rm d}$= -14 (dash-dotted line).

Fig. 9. Predicted d-component of the output impedance with HPF, $R_{\rm d}$= -5 (solid line), $R_{\rm d}$= -10 (dashed line) and $R_{\rm d}$= -14 (dash-dotted line), $\omega_{\rm cutoff} = 0.5\omega_{\rm res}$.

dB to 8 dB. However, the output impedance is impaired and decreases below the 0 dB line if the active damping feedback gain is set to $R_{\rm d} = 27$, which is near the maximum limit as shown in Fig. 4(a). Moreover, the output impedance loses its passive characteristics, i.e. the phase $\theta \notin [-90°, +90°]$.

The current control stability can be improved by applying a high-pass filter along the feedback path of the capacitor current measurement [34]. Accordingly, Fig. 7 presents the d-component of the output impedance when $f_{\rm res} < f_{\rm s}/6$ with $R_{\rm d} = [5, 15, 27]$. The HPF cutoff frequency was chosen as $\omega_{\rm cutoff} = \omega_{\rm res}$. As shown, the output impedance magnitude at the resonant frequency is significantly increased compared to the case with proportional capacitor current feedback. As a result, grid-voltage harmonics at the resonant frequency are mitigated more effectively. Additionally, the phase of the output impedance is passive even with larger virtual resistor values.

Considering root trajectories presented in Fig. 4, the output impedance magnitude at the resonant frequency is highest when the roots are farthest in the LHP from the imaginary-axis. This should be taken into account when determining the proper AD feedback gain for optimum output impedance magnitude at the resonant frequency.
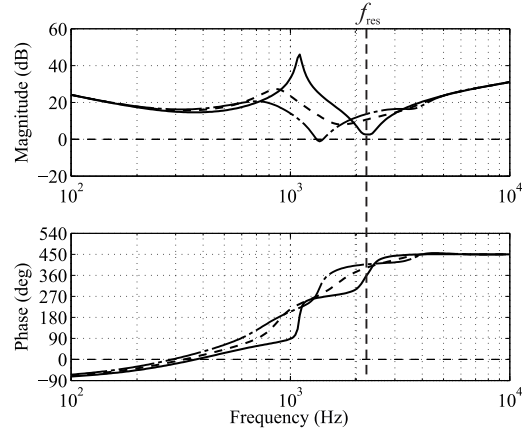
B. Output Impedance for $f_{\rm res} > f_{\rm s}/6$

Fig. 8 presents the predicted output impedance using proportional AD feedback when $f_{\rm res} > f_{\rm s}/6$ and $R_{\rm d} = [-5, -10, -14]$. Note that when operating under $f_{\rm res} > f_{\rm s}/6$ the active damping feedback gain has to be negative [7]. The magnitude of the impedance at the resonant frequency changes similarly as in Fig. 6 for $f_{\rm res} < f_{\rm s}/6$. However, the output impedance is not passive in aforementioned frequency range and, therefore, possibility for high-frequency impedance-based interactions is present [15].

Fig. 9 presents the output impedance with HPF AD using $\omega_{\rm cutoff} = 0.5\omega_{\rm res}$ and $R_{\rm d} = [-5, -10, -14]$. Comparing Figs. 8 and 9, it is evident that the HPF impairs the output impedance at the resonant frequency as the magnitude remains below the 0 dB line with all virtual resistor values and, therefore, voltage harmonics at the resonant frequency will easily affect the grid current. Moreover, the phase behavior remains non-passive and makes the grid-interface prone to impedance-based interactions.

In contrast, the output impedance can be improved by low-pass-filtering the capacitor current since the resonant frequency lies within $f_{\rm s}/6 < f_{\rm res} < f_{\rm s}/3$. Generally, the low-pass filter
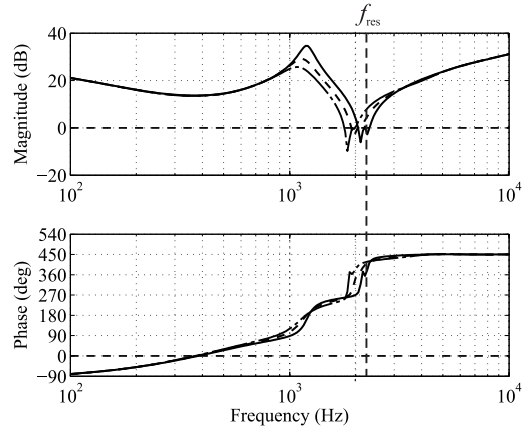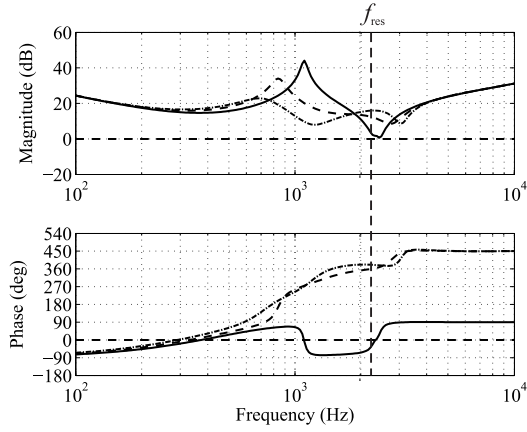
Fig. 10. Predicted d-component of the output impedance with LPF, R_d = -5 (solid line), R_d = -10 (dashed line) and R_d = -14 (dash-dotted line), $\omega_{\text{cutoff}} = \omega_{\text{res}}$.
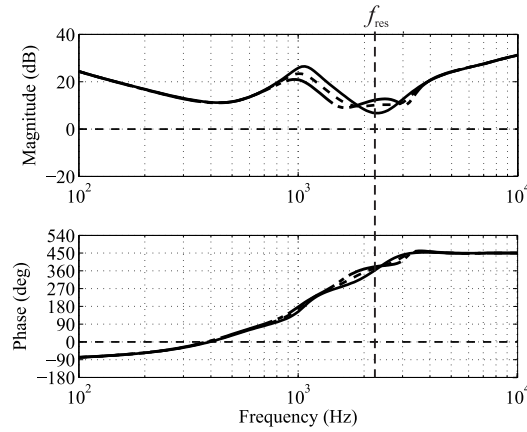

Fig. 11. Predicted d-component of the output impedance with HPF, R_d = -10 (solid line), R_d = -15 (dashed line) and R_d = -20 (dash-dotted line), $\omega_{\text{cutoff}} = 0.5\omega_{\text{res}}$.

can be presented in s-domain as $G_{\text{LPF}} = \omega_{\text{cutoff}}/(s + \omega_{\text{cutoff}})$, where ω_{cutoff} is the desired cutoff frequency. Fig. 10 shows the output impedance with $R_d = [-5, -10, -14]$ and $\omega_{\text{cutoff}} = 2\omega_{\text{res}}$. Clearly, the impedance magnitude is higher compared to impedances in Fig. 8 as the corresponding root trajectory in Fig. 4(f) also suggests. Moreover, the impedance behaves passively with low virtual resistor values and, therefore, the risk for impedance-based instability is decreased in that case.

For comparison, Fig. 11 shows the output impedance for $f_s/3 < f_{\text{res}} < f_s/2$ (f_s = 6 kHz) with high-pass-filtered capacitor current. As can be seen, the output impedance exhibits higher magnitude at the resonant frequency compared with the case in Fig. 9 for $f_s/6 < f_{\text{res}} < f_s/3$.

It can be, therefore, concluded that the HPF is unnecessary when $f_s/6 < f_{\text{res}} < f_s/3$ and should be omitted considering the output impedance magnitude as well as the overall converter stability. Instead, a low-pass filter in the capacitor current feedback should be used to increase the magnitude of the output impedance at the resonant frequency. Conversely, the HPF is recommended regarding the output impedance characteristics when $f_{\text{res}} < f_s/6$ and $f_s/3 < f_{\text{res}} < f_s/2$.
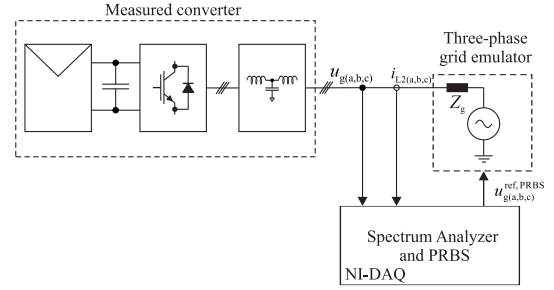

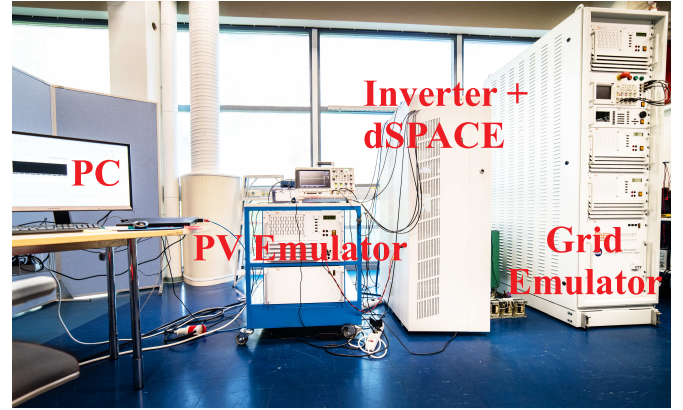Fig. 12. Overview of the device under test (DUT).

Fig. 13. The measurement setup.
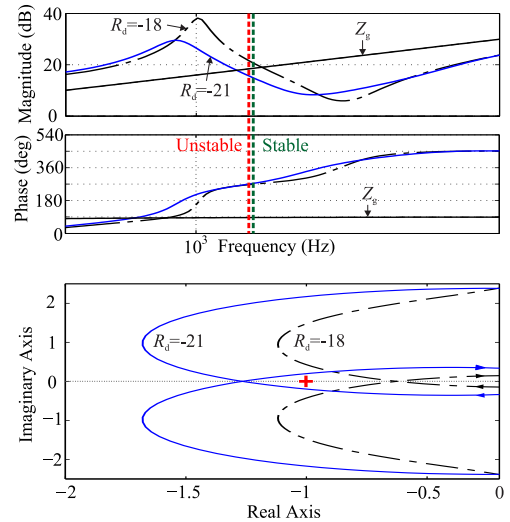
Fig. 14. Bode plots (upper figure) for Z_{odd}, Z_{g} and Nyquist diagram (lower figure) for the ratio of $Z_{\text{g}}/Z_{\text{odd}}$, $f_{\text{res}} > f_s/6$.

IV. EXPERIMENTAL RESULTS

The converter is susceptible to impedance-based instability if the phase of the output impedance is not passive. Furthermore, low output impedance at the resonant frequency enables the grid voltage harmonics to interact with the converter and cause harmonic currents proportional to the impedance magnitude at the corresponding frequency. These two factors may degrade the power quality to inadequate level. Therefore, it is important to address the aforementioned risks and include the output impedance analysis as a part of the active damping
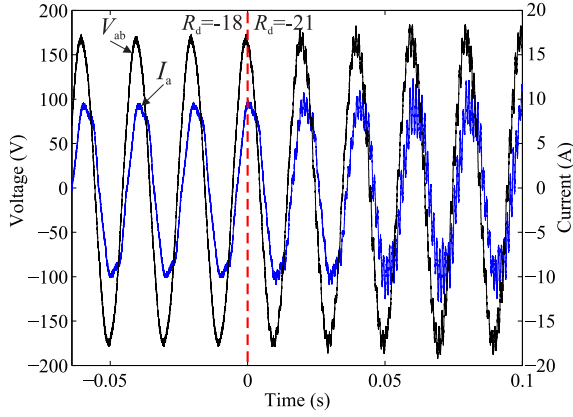
Fig. 15. Measured phase to phase voltage V_{ab} and phase current I_a with high-frequency impedance-based instability due to violation of Nyquist stability criterion in Fig. 14.
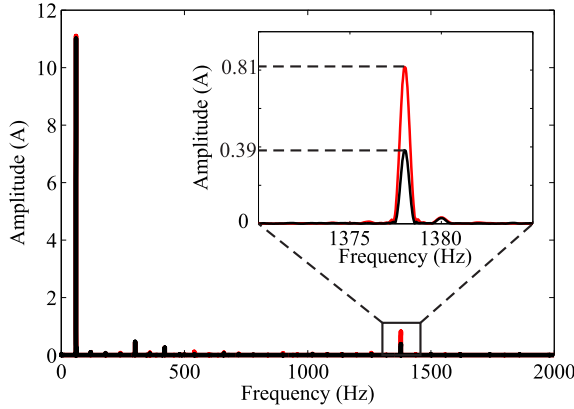

Fig. 16. Measured harmonic spectrum of the grid current with low impedance (red line) and high impedance (black line).
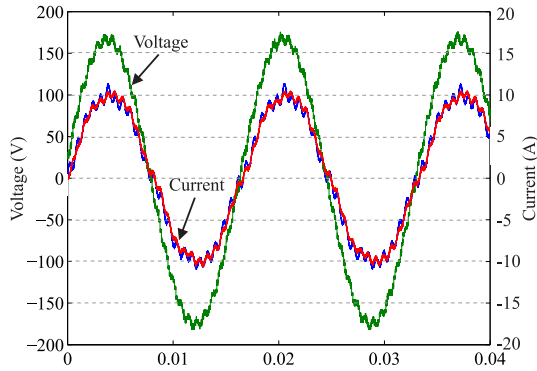

Fig. 17. Measured grid current response to grid voltage harmonics at the resonant frequency with high impedance (red line) and low impedance (blue line).

design. This section will verify the power quality issues induced by the impedance-based instability and low impedance magnitude. Moreover, the output impedances are measured for different active damping implementations to verify the accuracy of the model.

The measurement setup shown in Figs. 12 and 13 was implemented. Photovoltaic (PV) simulator PVS7000 and three-phase grid-emulator PAS15000 manufactured by Spitzenberger

& Spies are used as the power source and load, respectively. For power conversion, a SiC-based inverter MWINV-1044-SIC manufactured by MyWay is utilized. Converter control, omitted from Fig. 12 for simplicity, was implemented using a dSPACE DS1130 platform. Furthermore, the output impedance was measured with National Instruments Data Acquisition (DAQ) board using PRBS method [36].

Considering the impedance-based stability, Fig. 14 shows the bode plots for inductive grid impedance Z_g and non-passive output impedance Z_{odd} with LPF AD when $f_{res} = 8$ kHz $> f_s/6$. Moreover, Nyquist plot of the impedance ratio Z_g/Z_{odd} is shown. The d and q-component impedances are assumed to be decoupled in this case. A weak (high impedance) grid was demonstrated here with resistive and inductive values of $R = 0.5\Omega$ and $L = 1$mH, respectively. Accordingly, the Nyquist plot encircles the $(-1, 0)$ point when the virtual resistor value is decreased from $R_d = -18$ to $R_d = -21$, which leads to harmonic instability (Fig. 15). This can be correspondingly seen from the Bode plots as the phase difference exceeds 180 degrees when $|Z_g| > |Z_{odd}|$. Afore-mentioned impedance-based interaction sensitivity should be analyzed carefully when $f_{res} > f_s/6$ since the phase of the output impedance is naturally non-passive due to the delay.

In multi-parallel inverter systems, the voltage at the point-of-common-coupling (PCC) can be distorted due to reso-nant interaction between converters [27]. Therefore, the PCC voltage may contain harmonics near the LCL-filter resonant frequency, which can cause oscillation in the grid current. In order to analyze the harmonic rejection capability of the converter, high frequency harmonic injection (5 V ampli-tude, $f_{harmonic} = 1378$ Hz) was added to the grid-voltage reference which was then fed to the grid-emulator. This setup demonstrates a grid with elevated harmonic content. For the measurements, the output impedance magnitude of the converter was modified by adjusting the active damping gain in order to present two different cases. Accordingly, the lowest magnitude of the output impedance was set to 10 dB ≈ 3.2 Ω and the highest to 18 dB ≈ 7.9 Ω. A grid current spectrum was measured from an online system by using an oscilloscope and is presented in Fig. 16. Evidently, the grid-voltage harmonic causes large harmonic current if the impedance is low. However, by increasing the output impedance, the amplitude of the harmonic current is effectively decreased. Time-domain measurements of the corresponding case are shown in Fig. 17.

The output impedance predictions are verified with fre-quency response measurements shown in Fig. 18. Cases for both $f_{res} > f_s/6$ and $f_{res} < f_s/6$ are shown. The measured impedances match well with the analytical predictions. Thus, the model is suitable for accurately assessing the converter robustness against the grid voltage harmonics as well as evaluating the risk for impedance-based instability.

V. CONCLUSION

This paper presents an accurate small-signal impedance model for a three-phase ICF converter with capacitor-current-feedback active damping in the dq-domain. The effect of active
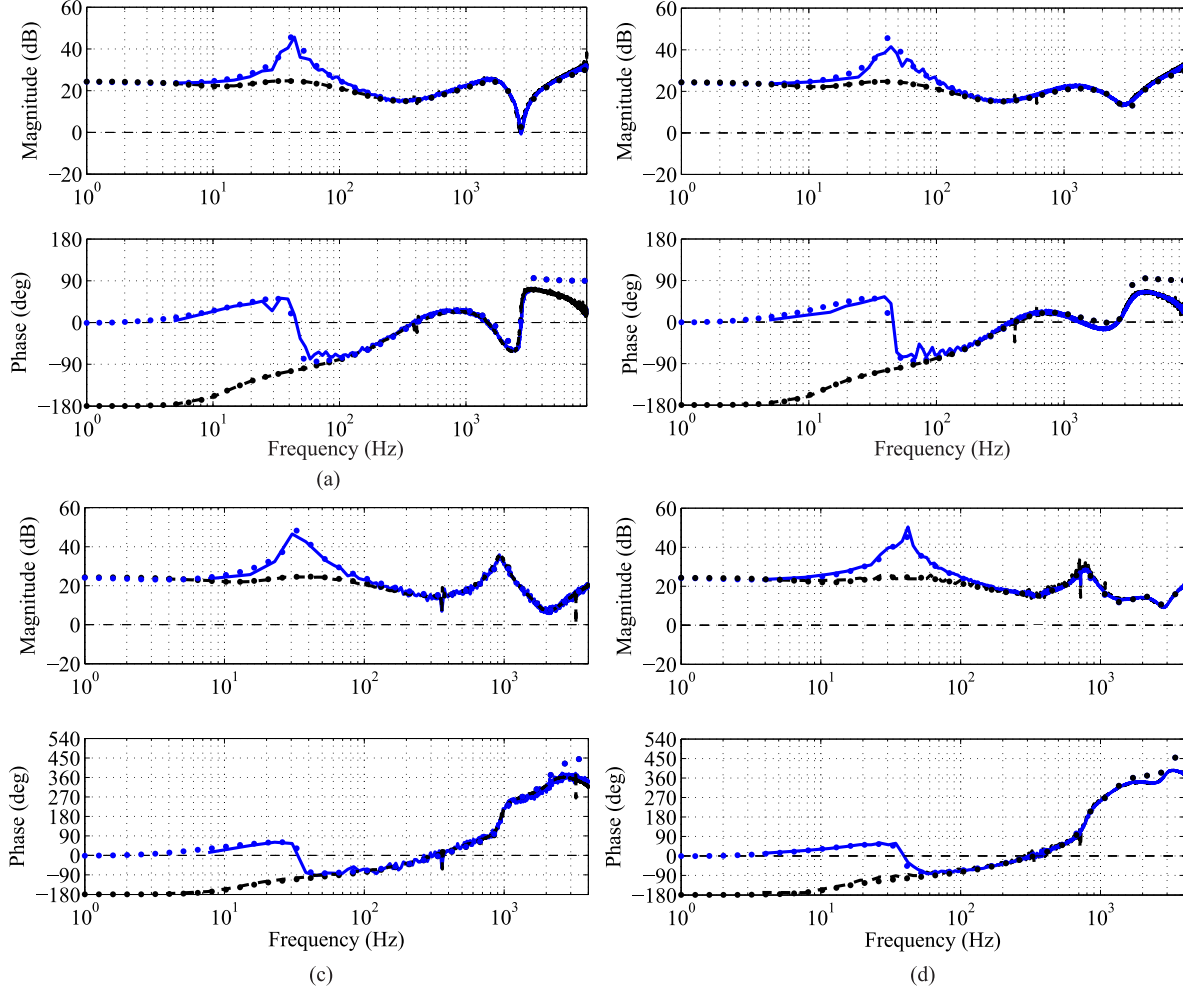
Fig. 18. Predicted (dotted lines) and measured d-and q-components (blue solid and black dashed lines, respectively) of the output impedances with different active damping implementations: (a) $f_{\mathrm{res}} < f_{\mathrm{s}}/6$, proportional AD feedback, $R_{\mathrm{d}} = 10$; (b) $f_{\mathrm{res}} < f_{\mathrm{s}}/6$, HPF AD feedback, $R_{\mathrm{d}} = 15$; (c) $f_{\mathrm{res}} > f_{\mathrm{s}}/6$, proportional AD feedback, $R_{\mathrm{d}} = -10$; (d) $f_{\mathrm{res}} > f_{\mathrm{s}}/6$, LPF AD feedback, $R_{\mathrm{d}} = -20$.

damping on the output impedance is thoroughly addressed which has not been done yet in literature. Accordingly, active damping design guidelines for effective shaping of the output impedance are presented considering the harmonic rejection capability and impedance-based stability. Moreover, it is shown that different active damping implementations have to be used depending on the ratio of the LCL-filter resonant and system sampling frequencies in order to improve the system performance. The developed impedance model can be used to intuitively address the stability of grid-interfaced converter with active damping, thus, minimizing the risks for high-frequency impedance-based instability and harmonic resonances. The output impedance characteristics were verified with 3-kW prototype inverter. The measurement results validate the accuracy of the impedance model.

APPENDIX A

The system state matrices presented in Section II in (1) are given as follows. In **A**-**D**, r_{eq} is the combined inverter-side inductor ESR and the switch on-time resistance, r_{C} is the LCL-filter capacitor ESR, r_{L2} is the grid-inductor ESR, C_{in} is

the input filter capacitor, L_1 is the inverter-side inductance, L_2 is the grid-side inductance, C_{f} is the LCL-filter capacitance, U_{in} is the steady-state input voltage, I_{in} is the steady-state input current, D_{d} is the d-component of the steady-state duty ratio, D_{q} is the q-component of the steady-state duty ratio and ω_{s} is the grid fundamental frequency.

$$
\mathbf{A} = \begin{bmatrix}
-\frac{r_{\mathrm{eq}}}{L_1} & \omega_{\mathrm{s}} & \frac{r_{\mathrm{C}}}{L_1} & 0 & -\frac{1}{L_1} & 0 & \frac{D_{\mathrm{d}}}{L_1} \\
-\omega_{\mathrm{s}} & -\frac{r_{\mathrm{eq}}}{L_1} & 0 & \frac{r_{\mathrm{C}}}{L_1} & 0 & -\frac{1}{L_1} & \frac{D_{\mathrm{q}}}{L_1} \\
\frac{r_{\mathrm{C}}}{L_2} & 0 & -\frac{r_{\mathrm{L2}}+r_{\mathrm{C}}}{L_2} & \omega_{\mathrm{s}} & \frac{1}{L_2} & 0 & 0 \\
0 & \frac{r_{\mathrm{C}}}{L_2} & -\omega_{\mathrm{s}} & -\frac{r_{\mathrm{L2}}+r_{\mathrm{C}}}{L_2} & 0 & \frac{1}{L_2} & 0 \\
\frac{1}{C_{\mathrm{f}}} & 0 & -\frac{1}{C_{\mathrm{f}}} & 0 & 0 & \omega_{\mathrm{s}} & 0 \\
0 & \frac{1}{C_{\mathrm{f}}} & 0 & -\frac{1}{C_{\mathrm{f}}} & -\omega_{\mathrm{s}} & 0 & 0 \\
-\frac{3}{2}\frac{D_{\mathrm{d}}}{C_{\mathrm{in}}} & -\frac{3}{2}\frac{D_{\mathrm{q}}}{C_{\mathrm{in}}} & 0 & 0 & 0 & 0 & 0
\end{bmatrix} \quad (17)
$$

$$\mathbf{B} = \begin{bmatrix} 0 & 0 & 0 & \frac{U_{\text{in}}}{L_1} & 0 \\ 0 & 0 & 0 & 0 & \frac{U_{\text{in}}}{L_1} \\ 0 & -\frac{1}{L_2} & 0 & 0 & 0 \\ 0 & 0 & -\frac{1}{L_2} & 0 & 0 \\ 0 & 0 & 0 & 0 & 0 \\ 0 & 0 & 0 & 0 & 0 \\ \frac{1}{C_{\text{in}}} & 0 & 0 & -\frac{I_{\text{in}}}{D_{\text{d}}C_{\text{in}}} & 0 \end{bmatrix} \quad (18)$$

$$\mathbf{C} = \begin{bmatrix} 0 & 0 & 0 & 0 & 0 & 0 & 1 \\ 1 & 0 & 0 & 0 & 0 & 0 & 0 \\ 0 & 1 & 0 & 0 & 0 & 0 & 0 \\ 0 & 0 & 1 & 0 & 0 & 0 & 0 \\ 0 & 0 & 0 & 1 & 0 & 0 & 0 \end{bmatrix} \quad (19)$$

$$\mathbf{D} = \mathbf{0} \quad (20)$$

APPENDIX B

Transfer function matrices presented in Section III in (15) can be derived from Fig. 2 and can be given as follows:

$$\mathbf{T}_{\text{oi}}^{\text{out}} = \mathbf{T}_{\text{oi}} - \mathbf{G}_{\text{ci}}(\mathbf{I} + \mathbf{L}_{\text{out}})^{-1} \left[\mathbf{L}_{\text{out}}\mathbf{G}_{\text{cL}}{}^{-1}\mathbf{G}_{\text{oL}} \right.$$
$$\left. -\mathbf{L}_{\text{out}}\mathbf{G}_{\text{cL}}{}^{-1}\mathbf{I}_{\text{L1}}\mathbf{G}_{\text{PLL}} -\mathbf{D}\mathbf{G}_{\text{PLL}} \right] \quad (21)$$

$$\mathbf{G}_{\text{ci}}^{\text{out}} = \mathbf{G}_{\text{ci}}(\mathbf{I} + \mathbf{L}_{\text{out}})^{-1}\mathbf{L}_{\text{out}}\mathbf{G}_{\text{cL}}{}^{-1} \quad (22)$$

$$\mathbf{Y}_{\text{o}}^{\text{out}} = \mathbf{Y}_{\text{o}} - \mathbf{G}_{\text{co}}(\mathbf{I} + \mathbf{L}_{\text{out}})^{-1} \left[\mathbf{L}_{\text{out}}\mathbf{G}_{\text{cL}}{}^{-1}\mathbf{G}_{\text{oL}} \right.$$
$$\left. -\mathbf{L}_{\text{out}}\mathbf{G}_{\text{cL}}{}^{-1}\mathbf{I}_{\text{L1}}\mathbf{G}_{\text{PLL}} -\mathbf{D}\mathbf{G}_{\text{PLL}} \right] \quad (23)$$

$$\mathbf{G}_{\text{co}}^{\text{out}} = \mathbf{G}_{\text{co}}(\mathbf{I} + \mathbf{L}_{\text{out}})^{-1}\mathbf{L}_{\text{out}}\mathbf{G}_{\text{cL}}{}^{-1} \quad (24)$$

Matrices $\mathbf{D}$ and $\mathbf{I}_{\text{L1}}$ are gains for the steady state duty-ratio and inductor current. Matrix $\mathbf{G}_{\text{PLL}}$ contains the PLL transfer functions which can be expressed as [26]

$$\mathbf{G}_{\text{PLL}} = \begin{bmatrix} 0 & 0 \\ 0 & G_{\text{PLL}} \end{bmatrix}, \quad (25)$$

$$G_{\text{PLL}} = \frac{1}{U_{\text{od}}} \frac{L_{\text{PLL}}}{1 + L_{\text{PLL}}}, \quad (26)$$

$$L_{\text{PLL}} = -G_{\text{PI-PLL}} \frac{U_{\text{od}}}{s}, \quad (27)$$

$$G_{\text{PI-PLL}} = K_{\text{p}} + \frac{K_{\text{i}}}{s}. \quad (28)$$

For the PLL PI-controller, $K_{\text{p}} = 0.67$ and $K_{\text{i}} = 38.02$.

REFERENCES

[1] M. Liserre, F. Blaabjerg, and S. Hansen, "Design and control of an LCL-filter-based three-phase active rectifier," *IEEE Trans. Ind. Appl.*, vol. 41, DOI 10.1109/TIA.2005.853373, no. 5, pp. 1281–1291, Sep. 2005.

[2] V. Blasko and V. Kaura, "A novel control to actively damp resonance in input LC filter of a three-phase voltage source converter," *IEEE Trans. Ind. Appl.*, vol. 33, DOI 10.1109/28.568021, no. 2, pp. 542–550, Mar. 1997.

[3] D. Pan, X. Ruan, C. Bao, W. Li, and X. Wang, "Optimized controller design for LCL-type grid-connected inverter to achieve high robustness against grid-impedance variation," *IEEE Trans. Ind. Electron.*, vol. 62, DOI 10.1109/TIE.2014.2341584, no. 3, pp. 1537–1547, Mar. 2014.

[4] D. Pan, S. Member, X. Ruan, S. Member, and C. Bao, "Capacitor-current-feedback active damping with reduced computation delay for improving robustness of LCL-type grid-connected inverter," *IEEE Trans. Power Electron.*, vol. 29, DOI 10.1109/TPEL.2013.2279206, no. 7, pp. 3414–3427, Jul. 2014.

[5] X. Wang, C. Bao, X. Ruan, W. Li, and D. Pan, "Design considerations of digitally controlled LCL-filtered inverter with capacitor-current-feedback active damping," *IEEE Trans. Emerg. Sel. Topics Power Electron.*, vol. 2, DOI 10.1109/JESTPE.2014.2350262, no. 4, pp. 972–984, Dec. 2014.

[6] J. Dannehl, F. W. Fuchs, S. Hansen, and P. B. Thøgersen, "Investigation of active damping approaches for PI-based current control of grid-connected pulse width modulation converters with LCL filters," *IEEE Trans. Ind. Appl.*, vol. 46, DOI 10.1109/TIA.2010.2049974, no. 4, pp. 1509–1517, Jul. 2010.

[7] R. Peña-Alzola, M. Liserre, F. Blaabjerg, M. Ordonez, and Y. Yang, "LCL-filter design for robust active damping in grid-connected converters," *IEEE Trans. Ind. Informat.*, vol. 10, DOI 10.1109/TII.2014.2361604, no. 4, pp. 2192–2203, Nov. 2014.

[8] P. Dahono, Y. Bahar, Y. Sato, and T. Kataoka, "Damping of transient oscillations on the output LC filter of PWM inverters by using a virtual resistor," in *Proc. IEEE 4th Int. Conf. on Power Electron. and Drive Syst.*, DOI 10.1109/PEDS.2001.975347, 2001, pp. 403–407.

[9] S. G. Parker, B. P. McGrath, and D. G. Holmes, "Regions of active damping control for LCL filters," *IEEE Trans. Ind. Appl.*, vol. 50, DOI 10.1109/TIA.2013.2266892, no. 1, pp. 424–432, Jan. 2014.

[10] J. Wang, J. D. Yan, L. Jiang, and J. Zou, "Delay-dependent stability of single-loop controlled grid-connected inverters with LCL filters," *IEEE Trans. Power Electron.*, vol. 31, DOI 10.1109/TPEL.2015.2401612, no. 1, pp. 743–757, Jan. 2016.

[11] X. Li, X. Wu, Y. Geng, X. Yuan, C. Xia, and X. Zhang, "Wide damping region for LCL-type grid-connected inverter with an improved capacitor-current-feedback method," *IEEE Trans. Power Electron.*, vol. 30, DOI 10.1109/TPEL.2014.2364897, no. 9, pp. 5247–5259, Sep. 2015.

[12] X. Wang, F. Blaabjerg, and P. C. Loh, "Grid-current-feedback active damping for LCL resonance in grid-connected voltage source converters," *IEEE Trans. Power Electron.*, vol. 31, DOI 10.1109/TPEL.2015.2411851, no. 1, pp. 213 – 223, Jan. 2015.

[13] C. Zou, B. Liu, S. Duan, and R. Li, "Influence of delay on system stability and delay optimization of grid-connected inverters with LCL filter," *IEEE Trans. Ind. Informat.*, vol. 10, DOI 10.1109/TII.2014.2324492, no. 3, pp. 1775–1784, Aug. 2014.

[14] L. Jessen and F. W. Fuchs, "Modeling of inverter output impedance for stability analysis in combination with measured grid impedances," in *2015 6th IEEE PEDG*, DOI 10.1109/PEDG.2015.7223037, Jun. 2015, pp. 1–7.

[15] J. Sun, "Impedance-based stability criterion for grid-connected inverters," *IEEE Trans. Power Electron.*, vol. 26, DOI 10.1109/TPEL.2011.2136439, no. 11, pp. 3075–3078, Nov. 2011.

[16] L. Harnefors, A. G. Yepes, A. Vidal, and J. Doval-Gandoy, "Passivity-based controller design of grid-connected VSCs for prevention of electrical resonance instability," *IEEE Trans. Ind. Electron.*, vol. 62, DOI 10.1109/TIE.2014.2336632, no. 2, pp. 702–710, Feb. 2015.

[17] M. Cespedes and J. Sun, "Impedance modeling and analysis of grid-connected voltage-source converters," *IEEE Trans. Power Electron.*, vol. 29, DOI 10.1109/TPEL.2013.2262473, no. 3, pp. 1254–1261, Mar. 2014.

[18] D. Yang, X. Ruan, and H. Wu, "Impedance shaping of the grid-connected inverter with LCL filter to improve its adaptability to the weak grid condition," *IEEE Trans. Power Electron.*, vol. 29, DOI 10.1109/TPEL.2014.2300235, no. 11, pp. 5795–5805, Nov. 2014.

[19] B. Wen, D. Dong, D. Boroyevich, R. Burgos, P. Mattavelli, and Z. Shen, "Impedance-based analysis of grid-synchronization stability for three-phase paralleled converters," *IEEE Trans. Power Electron.*, vol. 31, DOI 10.1109/TPEL.2015.2419712, no. 1, pp. 26–38, Jan. 2016.

[20] L. Harnefors, X. Wang, A. Yepes, and F. Blaabjerg, "Passivity-based stability assessment of grid-connected VSCs - An overview," *IEEE Trans. Emerg. Sel. Topics Power Electron.*, vol. 4, DOI 10.1109/JESTPE.2015.2490549, no. 1, pp. 116 – 125, Mar. 2016.

[21] B. Wen, D. Boroyevich, R. Burgos, P. Mattavelli, and Z. Shen, "Analysis of D-Q small-signal impedance of grid-tied inverters," *IEEE Trans. Power Electron.*, vol. 31, DOI 10.1109/TPEL.2015.2398192, no. 1, pp. 675–687, Jan. 2016.

[22] X. Wu, X. Li, X. Yuan, and Y. Geng, "Grid harmonics suppression scheme for LCL-type grid-connected inverters based on output admittance revision," *IEEE Trans. Sustain. Energy*, vol. 6, DOI 10.1109/TSTE.2014.2384509, no. 2, pp. 411–421, Apr. 2015.

[23] X. Chen, Y. Zhang, S. Wang, J. Chen, and C. Gong, "Impedance-phased dynamic control method for grid-connected inverters in a weak grid," *IEEE Trans. Power Electron.*, vol. 32, DOI 10.1109/TPEL.2016.2533563, no. 1, pp. 274–283, Jan. 2017.

[24] Y. Yu, H. Li, and Z. Li, "Impedance modeling and stability analysis of lcl-type grid-connected inverters with different current sampling schemes," in *2016 IEEE 8th IPEMC-ECCE Asia*, DOI 10.1109/IPEMC.2016.7512419, May. 2016, pp. 974–981.

[25] X. Wang, Y. W. Li, F. Blaabjerg, and P. C. Loh, "Virtual-impedance-based control for voltage-source and current-source converters," *IEEE Trans. Power Electron.*, vol. 30, DOI 10.1109/TPEL.2014.2382565, no. 12, pp. 7019–7037, Dec. 2015.

[26] T. Messo, J. Jokipii, A. Mäkinen, and T. Suntio, "Modeling the grid synchronization induced negative-resistor-like behavior in the output impedance of a three-phase photovoltaic inverter," in *Proc. 4th IEEE PEDG*, DOI 10.1109/PEDG.2013.6785602, Jul. 2013, pp. 1–7.

[27] J. L. Agorreta, M. Borrega, J. Lopez, and L. Marroyo, "Modeling and control of N-paralleled grid-connected inverters with LCL filter coupled due to grid impedance in pv plants," *IEEE Trans. Power Electron.*, vol. 26, DOI 10.1109/TPEL.2010.2095429, no. 3, pp. 770–785, Mar. 2011.

[28] J. He and Y. W. Li, "Generalized closed-loop control schemes with embedded virtual impedances for voltage source converters with LC or LCL filters," *IEEE Trans. Power Electron.*, vol. 27, DOI 10.1109/TPEL.2011.2168427, no. 4, pp. 1850–1861, Apr. 2012.

[29] Y. Li, P. Jia, and T. Q. Zheng, "Active damping method to reduce the output impedance of the dc-dc converters," *IET Power Electron.*, vol. 8, DOI 10.1049/iet-pel.2013.0911, no. 1, pp. 88–95, Aug. 2015.

[30] A. Aapro, T. Messo, and T. Suntio, "An accurate small-signal model of a three-phase VSI-based photovoltaic inverter with LCL-filter," in *Proc. IEEE 9th Int. Conf. on Power Electron. and ECCE Asia*, DOI 10.1109/ICPE.2015.7168092, 2015, pp. 2267–2274.

[31] I. Cvetkovic, M. Jaksic, D. Boroyevich, P. Mattavelli, F. Lee, Z. Shen, S. Ahmed, and D. Dong, "Un-terminated, low-frequency terminal-behavioral dq model of three-phase converters," in *Proc. IEEE Energy Conv. Congr. and Expo.*, DOI 10.1109/ECCE.2011.6063851, 2011, pp. 791–798.

[32] S. Buso and P. Mattavelli, *Digital Control in Power Electronics*. San Francisco, CA, USA: Morgan & Claypool, 2006.

[33] R. Peña-Alzola, M. Liserre, F. Blaabjerg, R. Sebastián, J. Dannehl, and F. W. Fuchs, "Systematic design of the lead-lag network method for active damping in LCL-filter based three phase converters," *IEEE Trans. Ind. Informat.*, vol. 10, DOI 10.1109/TII.2013.2263506, no. 1, pp. 43–52, Feb. 2014.

[34] X. Wang, F. Blaabjerg, and P. C. Loh, "Virtual rc damping of LCL-filtered voltage source converters with extended selective harmonic compensation," *IEEE Trans. Power Electron.*, vol. 30, DOI 10.1109/TPEL.2014.2361853, no. 9, pp. 4726–4737, Sep. 2015.

[35] T. Messo, A. Aapro, and T. Suntio, "Generalized multivariable small-signal model of three-phase grid-connected inverter in dq-domain," in *Proc. IEEE 16th Workshop on Control and Modeling for Power Electron.*, DOI 10.1109/COMPEL.2015.7236460, 2015, pp. 1–8.

[36] T. Roinila, J. Huusari, and M. Vilkko, "On frequency-response measurements of power-electronic systems applying MIMO identification techniques," *IEEE Trans. Ind. Electron.*, vol. 60, DOI 10.1109/TIE.2012.2221118, no. 11, pp. 5270–5276, Nov. 2013.